Construction and Building Materials 168 (2018) 91–104

Contents lists available at ScienceDirect

Construction and Building Materials

journal homepage: www.elsevier.com/locate/conbuildmat

Evaluation of pavement layer thicknesses using GPR: A comparison between full-wave inversion and the straight-ray method

Albéric De Coster [a,*], Audrey Van der Wielen [b], Colette Grégoire [b], Sébastien Lambot [a]

[a] Université catholique de Louvain, Earth and Life Institute, Croix du Sud 2, Box L7.05.02, 1348 Louvain-la-Neuve, Belgium
[b] Belgian Road Research Centre, Boulevard de la Woluwe 42, 1200 Brussels, Belgium

HIGHLIGHTS

- Estimation of the electromagnetic and physical properties of pavements.
- Analysis of the capabilities of the surface reflection coefficient and full-wave inversion methods.
- Fast and good results provided by the surface reflection coefficient approach.
- Wider range of configurations and smaller errors provided by the full-wave inversion approach.
- Adequate processing steps required before inverting the data with both inversion methods.

ARTICLE INFO

Article history:
Received 15 December 2017
Received in revised form 8 February 2018
Accepted 15 February 2018

Keywords:
Full-wave inversion (FWI)
Ground-penetrating radar (GPR)
Pavement characterization
Surface reflection coefficient (SRC)
Thickness estimation

ABSTRACT

The characterization of pavement properties is essential to manage transport infrastructures. In this paper, we aim at assessing the abilities of the ground-penetrating radar (GPR) full-wave inversion and straight-ray methods to achieve this task. The first approach consists in combining a full-wave-inversion procedure with a recently developed electromagnetic model. The latter takes advantage of a closed-form solution of Maxwell's equations to describe the antenna-medium system. The second approach resorts to the surface reflection coefficient method. We showed through numerical experiments that the straight-ray method in general provides fast and good results, but full-wave inversion applies to a wider range of model configurations and is subject to less important errors. A laboratory experiment was also conducted to take into account the effects of measurement errors as well as inherent pavement heterogeneities. The results evidence that noisy data and a lack of information can sometimes lead to an inappropriate estimation of the parameters. Nonetheless, applying an adequate processing before inverting the data made both inversion methods able to provide an estimation of the pavement thickness along the acquisition profile.

1. Introduction

All over the world, transportation infrastructures constitute a sector to which a major part of public investments is allocated [1]. In their lifetime, which has to be maximized, the infrastructures have to guarantee safety and comfort to the users [2]. The characterization of the structure and physical properties of the pavement is therefore essential to plan the maintenance of road networks. Currently, most administration agencies mainly resort to the extraction of pavement cores or trial pits to achieve this task [3]. Even though this procedure enables to acquire relatively accurate results, it is destructive, expensive and time-consuming. Furthermore, it requires traffic disruptions and provides only limited information as the method does not take into account the spatial and temporal variability of the structural and physical properties of the road layers [3–5].

Ground-penetrating radar (GPR) is a non-destructive tool that has raised a substantial interest in pavement investigations [6,7] and that has greatly evolved since the first radar road surveys in the mid-70's. This success has mainly arisen from the non-invasive and high-resolution characterization of pavements, which overcomes the drawbacks previously cited. Regarding pavement investigation, this tool has been considered as reliable for void detection [8], water content estimation [5,9–11], density estimation [12,13], pavement distresses assessment [14,15] and concrete structures monitoring [16–18].

* Corresponding author.
E-mail address: alberic.decoster@uclouvain.be (A. De Coster).

https://doi.org/10.1016/j.conbuildmat.2018.02.100
0950-0618/

The determination of the thickness of the transport infrastructure layers is one of the various road applications to which GPR has been successfully and most commonly dedicated [6,19–21]. For newly built pavements, accurate predictions of the layer thicknesses are needed to carry out quality controls and check their conformity. For older pavements, the thickness estimated from GPR measurements can be integrated in falling weight deflectometer (FWD) data processing in order to calculate the layer moduli [22,23] and predict the remaining lifetime. The type of rehabilitation (overlay or structural repair) can be deduced from those investigations [3,4,24–26].

The estimation of the layer thickness requires an accurate knowledge of the pavement relative permittivity. Several calibration approaches have been used to assign values to pavement dielectric properties [20,27,28]. The easiest one consists in resorting to generic published values but the results may be inaccurate because we neglect particular in situ conditions. Errors up to 20% in thickness calculation are generated by errors up to 50% in permittivity [29]. Core/trench drilling is another method commonly applied to determine pavement thickness. In that respect, two strategies can be adopted based on pavement samples. The first one involves laboratory measurements using a suitable test system [20,30] whereas the second one, referred to as the travel time-core thickness procedure, correlates the GPR data with those of the physical samples [20,31]. The accurate estimation of the permittivity obtained at the core/trench location is afterwards used to predict its value for the rest of the profile. This destructive approach therefore implies the major limitations previously mentioned.

To overcome these issues, non-destructive alternatives showing fast and high-resolution estimation of the dielectric constant value have been developed. The most popular one is the surface reflection coefficient (SRC) method. This approach compares the amplitude of the signal reflected by a perfect electrical conductor placed on the pavement surface to the amplitude of the reflected signal coming from the investigated surface [32]. The error associated with this approach varies depending on the study-case. For example, Al-Qadi et al. [33] conducted GPR surveys to measure the thicknesses of the layers of a newly built pavement and found a mean thickness error of 2.9% for hot-mix asphalt (HMA) layers ranging between 100 and 250 mm. More recently, Zhao et al. [34] computed the thicknesses of asphalt concrete overlays with different layer thicknesses and mixture types by resorting to the surface reflection method and a regularized deconvolution. They compared their results to ground truths and obtained a maximum error of 4.2%.

Once the surface layer permittivity is computed, an iterative process can be applied in order to estimate the same property for a certain number of underlying layers [3,19]. Loizos and Plati [20] compared this approach with the travel time-core thickness procedure and laboratory results on asphalt concrete pavements. The study reported an average error oscillating between 5% and 10% depending on the method used to determine the dielectric constant. They highlighted that the surface reflection coefficient (SRC) method constitutes a good trade-off between accuracy and effectiveness. Li et al. [25] also took benefits from this methodology and combined it with a layer picking algorithm to successfully estimate the thickness of the successive pavement layers. The formulation of this iterative approach assumes that the permittivities assigned at the material interfaces do not vary within the layer. The attenuation may be either neglected or roughly taken into account, based on the material conductivity estimated by the user [3]. Even if these assumptions have been proven to work reasonably for strong air-surface reflection, it is worth noting that they can inherently reduce the accuracy of the estimates regarding the thickness of the underlying pavement layers [19]. This statement is especially true for investigations led over old, degraded or wet pavements [28].

Multi-offset approaches are another set of methods which avoids physical samplings as well as the misalignment with respect to cores. They are applicable in near-field conditions contrary to the previously described approach. It also allows deriving the full velocity cross-section [28] as the velocity of the electromagnetic waves within each individual layer is characterized [9,35]. For example, Fauchard et al. [30] tested the common midpoint (CMP) technique and showed that its accuracy remained below the road facility manager requirements. Lahouar et al. [36] used a modified CMP technique to estimate the thickness based on GPR data collected along an interstate section. The authors reported a thickness error varying between 1% and 15% with a mean error of 6.8%. Several other extended CMP methods have been developed to enhance the accuracy of the pavement permittivity estimation [21,37]. More recently, Liu and Sato [38]) presented a new ground-coupled GPR system with a common source antenna array to measure the permittivity and the thickness of the pavement layers. The quantitative inspection of an in situ asphalt pavement led to a thickness estimation error lower than 10%. Another work resorted to two air-coupled horn antennas and a wide-angle reflection and refraction (WARR) acquisition procedure to deduce the parameters of the surface layer [29].

With the ever increasing power of computers, full-wave inversion (FWI) has become an applicable tool to derive quantitative material properties from GPR data [39]. Compared to the other methods, the FWI approach maximizes the information retrieval capabilities by taking advantage of the whole recorded signal as well as by involving an electromagnetic model with a minimum of simplifying hypotheses. The FWI scheme applied on off-ground GPR has demonstrated excellent potentialities, whether it is to retrieve electromagnetic properties and thicknesses of multi-layered concrete media [40,41] or to estimate and map the soil water content at the field scale [42,43]. Yet, few applications using FWI have been dedicated to road applications [44,45]. Cao et al. [45] simulated full-waveform GPR signals in far-field conditions over a wide range of pavement profiles and developed a successful interpretation scheme to estimate the thicknesses of the layers without a priori assumptions of the pavement condition. They found a thickness error below 7% for 80 to 130 mm asphalt layers arranged over the base material. Nonetheless, like all the approaches previously presented, potential depth miscalculations and wrong estimates of the electromagnetic parameters could arise from the simplifying assumptions related to the electromagnetic wave propagation phenomena and the characterization of the antenna properties [46]. Mahmoudzadeh et al. [47] proposed a methodology in order to address these issues and retrieve the physical and electromagnetic properties of the road for both asphalt and basement layers. The approach is based on the electromagnetic model developed by Lambot et al. [46] and is valid for far-field conditions. Even if full-wave inversion for near-field GPR data is now available [48–50], it has not been assessed yet for road inspection.

In this study, we compare the surface reflection coefficient and full-wave inversion methods to reconstruct pavement properties. In the first approach, which is commonly used by road administration agencies, we use the peak-to-peak amplitude analysis in the time domain to estimate the pavement properties. In the second approach, we resort to the near-field full-wave model recently introduced by Lambot and André [51] to achieve the same goal. This model, which is a generalization of the previously developed far-field model [46], intrinsically describes the radar antennas using global reflection and transmission characteristic functions [51,52]. We conducted numerical and laboratory experiments in order to test these two approaches and compare their abilities to provide information about the spatial variability of the pavement physical and electromagnetic properties. It is worth noting that the test site involved in the laboratory experiment exhibits a quite complex configuration which includes noise and heterogeneities inherent to real-case surveys.

2. Layer thickness estimation methods

This section describes the inverse modeling strategies used to estimate the pavement properties, namely, the surface reflection coefficient (SRC) and the full-wave inversion (FWI) methods.

2.1. The surface reflection coefficient method

The surface reflection coefficient (SRC) method is an efficient approach which allows estimating the medium relative permittivity of the surface layer ($\varepsilon_{r,1}$). Knowing this electromagnetic property and assuming straight ray propagation, the thickness of the layer (h_1) can be determined using the following equation:

$$h_1 = \frac{c\Delta t}{2\sqrt{\epsilon_{r,1}}} \tag{1}$$

where c and Δt denote the speed of light in free space (3.10^8 m/s) and the two-way travel time of the wave propagating within the pavement layer, respectively. Eq. (1) assumes a low-loss layer, which appears to be quite reasonable for most of road materials in the GPR frequency range. The strategy adopted to compute $\varepsilon_{r,1}$ based on the SRC approach consists in comparing the amplitude of every measurement to a calibration measurement performed over a perfect reflector. During the calibration phase, the antenna is moved vertically, so that the reflection is measured for all the soil-antenna distances (Fig. 1a). Based on these measurements (Fig. 1b), a calibration file is created by calculating the mean trace of all the signals with the same reflection arrival time (Fig. 1c). For each arrival time, the incident amplitude A_{calib} is considered as the peak-to-peak amplitude of the perfect reflection (Fig. 2). After field measurements, the amplitude of the surface reflection A_0 is estimated for each trace and compared to the one measured over the metal plate for the same arrival time (A_{calib}). The reflection coefficient R_0 is then obtained by multiplying this quotient by -1, which permits to take into account the phase change generated by the reflection on the metal.

Based on the surface reflection coefficient R_0, the relative permittivity $\varepsilon_{r,1}$ can be calculated using the following equation [3,53]:

$$\varepsilon_{r,1} = \frac{(1-R_0)^2}{(1+R_0)^2} = \left(\frac{1+\frac{A_0}{A_{calib}}}{1-\frac{A_0}{A_{calib}}}\right)^2 \tag{2}$$

In this relationship, the incidence angle of the waves with respect to the surface is assumed to be 90°. This hypothesis is assumed to be valid when the distance between the receiving and the emitting antennas can be neglected compared to the soil-antenna distance. This method can be applied to derive the surface material permittivity from every measured trace if the soil-antenna distance is considered in the calibration procedure. However, errors in the estimates are expected if a gradient of properties is present (e.g., drying material). Moreover, if the surface layer thickness is too small compared to the wavelength, reflection interferences will be produced, which may lead to significant estimation errors [53,54]. To limit this phenomenon, we generally consider that the thickness should be larger than half the wavelength.

As explained above, the layer thickness can be estimated by identifying the reflection occurring at the interface between the two first road layers. This reflection is visible in the radargram if the permittivity contrast between the two materials is sufficiently strong. The estimation of the relative permittivity of the second layer is based on the amplitude of this second reflection. In many cases, this amplitude cannot be directly measured in the radargram because it is affected by the surface reflection. The strategy used to isolate the second reflection consists in generating a signal which only takes into account the surface reflection and subtracting its amplitude from the measurement. The computation of this synthetic signal is done by multiplying the corresponding calibration measurement by the reflection coefficient (Fig. 3). The maximum amplitude of the resulting signal is consequently supposed to correspond to the reflection coming from the bottom of the first layer. The peak-to-peak amplitude of this reflection A_1 can therefore be estimated. The reflection is recorded at a two-way travel time referred to as t_1.

The parameters A_1 and t_1 can be used to estimate the relative permittivity of the second layer using the following equation [3]:

$$\varepsilon_{r,2} = \varepsilon_{r,1}\left(\frac{\left(1-\left(\frac{A_0}{A_{calib}}\right)^2\right)e^{-\frac{\eta_0\sigma_1 t_1 c}{2\varepsilon_{r,1}}}+\left(\frac{A_1}{A_{calib}}\right)}{\left(1-\left(\frac{A_0}{A_{calib}}\right)^2\right)e^{-\frac{\eta_0\sigma_1 t_1 c}{2\varepsilon_{r,1}}}-\left(\frac{A_1}{A_{calib}}\right)}\right)^2 \tag{3}$$

where η_0 is the wave impedance of free space ($\eta_0 \approx 120\pi\ \Omega$) and σ_1 represents the conductivity of the first material. This conductivity cannot be calculated from the measured traces and has either to be assumed negligible or to be estimated by the user. Furthermore, the estimation of $\varepsilon_{r,2}$ in Eq. (3) suffers from the approximations made during the evaluation of $\varepsilon_{r,1}$ and t_1. Other assumptions are related to the SRC approach [53]: (1) the antennas are located in free space above a homogeneous half-space limited by a plane layered medium, (2) the reflection coefficient can be approximated by the plane wave reflection coefficient, (3) antenna distortion effects are negligible and (4) the relative permittivity is assumed to be

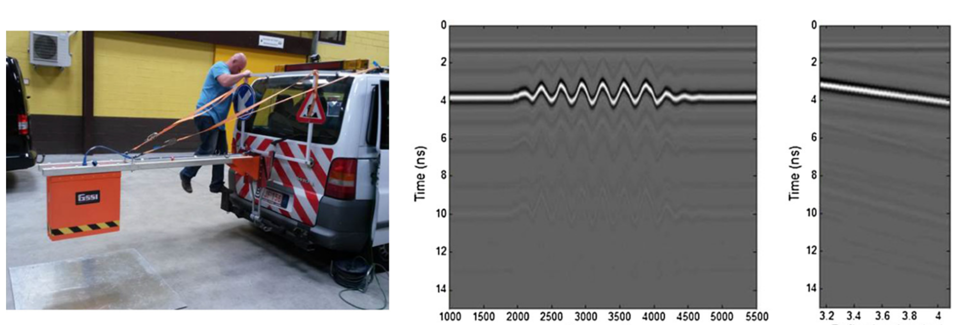

Fig. 1. (a) Calibration measurement, (b) profile measured during the calibration and (c) resulting calibration file.

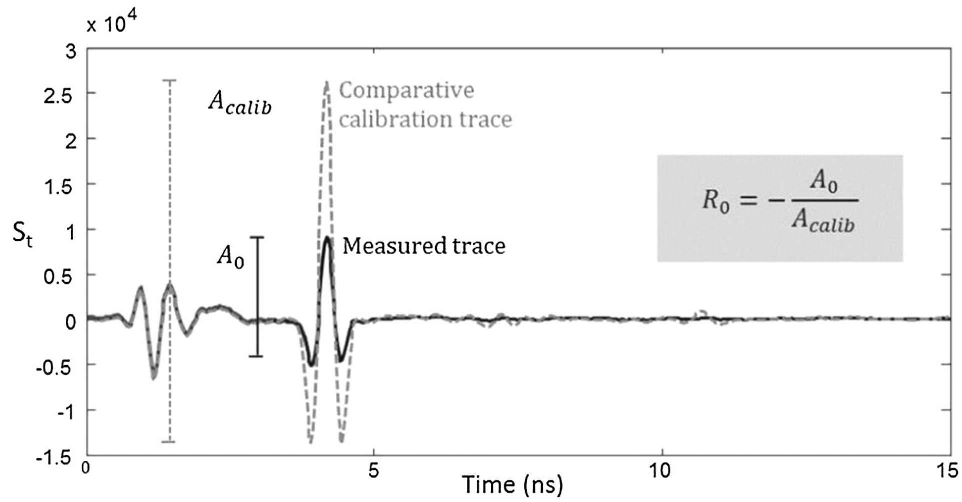

Fig. 2. Comparison of a measured trace with the comparative calibration trace (i.e., the trace presenting the same surface reflection time).

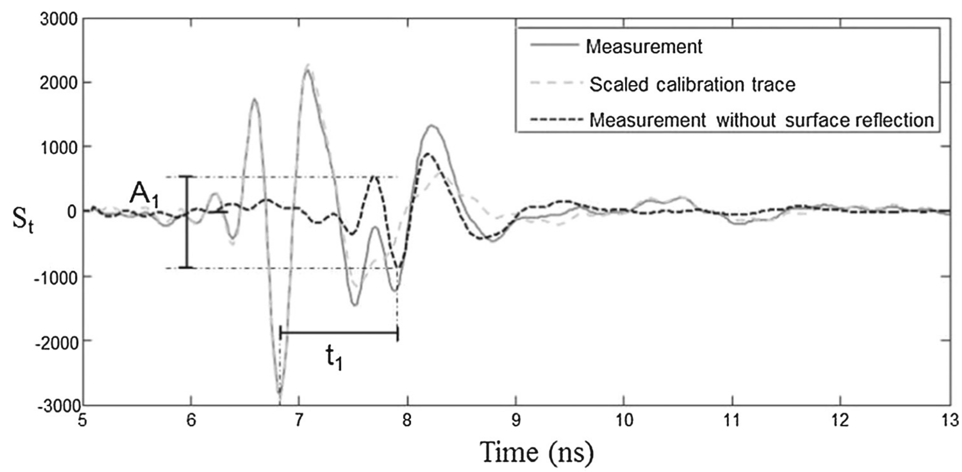

Fig. 3. Scaled calibration traces subtraction aiming at isolating the reflection accounting for the bottom of the first layer.

frequency-independent. A similar method can be used for all the underlying layers [3], but the precision of the results is expected to significantly decrease for each additional interface.

2.2. The full-wave inversion method

2.2.1. GPR full-wave model

The near-field model relies on a full-wave solution of the 3-D Maxwell's equations for wave propagation in antenna-medium systems [46,51]. When the antenna is relatively close to the medium, the distribution of the backscattered field over the antenna aperture depends on the antenna-medium distance and on the electromagnetic properties of the medium. In that case, the antenna is described using a series of point sources and receivers. The trade-off between the computation time and the accuracy of the model determines the number of source/field points that are required. Complex and frequency-dependent global transmission and reflection coefficients are used to characterize wave propagation between these source/field points and the radar reference plane. These coefficients permit to account for the variations of impedance within the antenna and the antenna-medium coupling. The link between the radar measurements, the antenna characteristics and the medium properties is expressed in the frequency domain as follows [51]:

$$S(\omega) = \frac{b(\omega)}{a(\omega)} = T_0(\omega) + \mathbf{T_s}\left(\mathbf{I_N} - \mathbf{G^0}\mathbf{R_s}\right)^{-1}\mathbf{G}\mathbf{T_i} \quad (4)$$

with

$$\mathbf{T_i} = [\,T_{i,1}(\omega) \quad T_{i,2}(\omega) \quad \cdots \quad T_{i,N}(\omega)\,]^T \quad (5)$$

$$\mathbf{T_s} = [\,T_{s,1}(\omega) \quad T_{s,2}(\omega) \quad \cdots \quad T_{s,N}(\omega)\,] \quad (6)$$

$$\mathbf{R_s} = \mathrm{diag}([\,R_{s,1}(\omega) \quad R_{s,2}(\omega) \quad \cdots \quad R_{s,N}(\omega)\,]) \quad (7)$$

$$\mathbf{G} = \begin{bmatrix} G_{11}(\omega) & G_{12}(\omega) & \cdots & G_{1N}(\omega) \\ G_{21}(\omega) & G_{22}(\omega) & \cdots & G_{2N}(\omega) \\ \vdots & \vdots & & \vdots \\ G_{N1}(\omega) & G_{N2}(\omega) & \cdots & G_{NN}(\omega) \end{bmatrix} \quad (8)$$

and

$$\mathbf{G^0} = \begin{bmatrix} G^0_{11}(\omega) & G^0_{12}(\omega) & \cdots & G^0_{1N}(\omega) \\ G^0_{21}(\omega) & G^0_{22}(\omega) & \cdots & G^0_{2N}(\omega) \\ \vdots & \vdots & & \vdots \\ G^0_{N1}(\omega) & G^0_{N2}(\omega) & \cdots & G^0_{NN}(\omega) \end{bmatrix} \quad (9)$$

where ω is the angular frequency, $S(\omega)$ denotes the ratio between the backscattered field $b(\omega)$ and the incident field $a(\omega)$ at the radar reference plane (i.e., the radar signal), I_N refers to the N-order identity matrix with N being the number of source/field points, $T_0(\omega)$ is the global transmission/reflection coefficient of the antenna and corresponds to the return loss within the antenna in free space, $T_{i_{..}}(\omega)$ is the transmission transfer function for the field incident from the radar reference plane onto the point source, $T_{s_{..}}(\omega)$ designates the transmission transfer function for the fields incident from the point source onto the radar reference plane and $R_{s_{..}}(\omega)$ denotes the global reflection coefficient for fields incident from the layered medium onto the field point and accounts for antenna-medium coupling. $G_{..}(\omega)$ and $G^0_{..}(\omega)$ are the transmitter–receiver and receiver-receiver Green's functions, respectively, and correspond to the exact solutions of the 3-D Maxwell's equations for wave propagation in planar multilayered media.

The computation of the antenna characteristic transfer functions presented in Eq. (4) involves near- and far-field radar measurements collected at different distances from a layered medium having well-known electromagnetic properties (e.g., perfect electrical conductor (PEC) or water). Knowledge of these antenna-medium distances and these properties enables the calculation of the layered Green's functions ($G_{..}(\omega)$ and $G^0_{..}(\omega)$) which, along with the radar signal ($S(\omega)$), are subsequently entered into Eq. (4). A complex numerical inverse modeling procedure is used to solve this non-linear optimization scheme and determine the antenna characteristic coefficients. More details about the calibration procedure can be found in Lambot and André [51].

2.2.2. Data inversion

The near-field model previously described is combined with a full-wave inversion procedure in order to retrieve the medium properties. The underlying strategy consists in simulating GPR signals based on different parameter vectors and to compare these ones to the measured signal. The inversion problem is formulated in the least-squares sense and the objective function to be minimized $\phi(\mathbf{P})$ is expressed as follows:

$$\phi(\mathbf{P}) = |\mathbf{S}^* - \mathbf{S}|^T |\mathbf{S}^* - \mathbf{S}| \tag{10}$$

where $\mathbf{P}$ corresponds to the vector containing the parameters to be estimated for each layer of the multilayered medium (i.e., the layer thickness h, the relative permittivity ε_r and the electrical conductivity σ), T denotes the transpose and $\mathbf{S} = S(\omega, \mathbf{P})$ and $\mathbf{S}^* = S(\omega)$ are the vectors gathering the simulated and observed GPR data, respectively. The inverse modeling procedure amounts to face a non-linear optimization scheme. This issue is tackled by resorting to the sequential combination of the Global Multilevel Coordinate Search (GMCS) algorithm [55] with the Nelder-Mead Simplex (NMS) algorithm [56]. This robust optimization approach enables us to efficiently explore intricate multi-dimensional objective function topographies and to identify the position of their respective global minimum.

3. Numerical experiments

3.1. Materials and methods

Numerical experiments were conducted in order to theoretically assess the capabilities of the SRC and FWI methods to estimate the thickness of pavement layers. We began by generating various signals considering the monolayer and bilayer configurations displayed in Fig. 4. For the first layout, we implemented different relative permittivity values ranging from 3 to 20 with a step equal to 1, resulting in 18 simulated signals. For the second layout, we generated 13965 different signals by attributing values to three different parameters, namely, the relative permittivity ($\varepsilon_{r,1}$) of the upper layer, its thickness (h_1) and the relative permittivity of the bottom layer ($\varepsilon_{r,2}$). The parameter combinations were evenly sampled in the following ranges of values: $\varepsilon_{r,1} = [3.0 : 0.5 : 13.0], h_1 = [0.010 : 0.005 : 0.100]$ and $\varepsilon_{r,2} = [3.0 : 0.5 : 20.0]$. We tested more values of permittivity for the second layer as this one can be potentially wetter than the surface layer. Whatever the chosen configuration and the selected parameter combinations, we resorted to the model of Ledieu et al. [57] to relate the material volumetric water content (θ) to its relative permittivity (ε_r), namely:

$$\theta = a.\sqrt{\varepsilon_r} + b \tag{11}$$

where we fixed a = 0.1264 and b = −0.1933. These parameters are assumed to show only small variations for a wide range of soils [58]. The model of Rhoades et al. [59] was then used to assign electrical conductivities (σ) to the layers:

$$\sigma = (c.\theta^2 + d.\theta).\sigma_w + \sigma_s \tag{12}$$

where the electrical conductivity of the water (σ_w) was fixed to 0.075 S/m [60], the electrical conductivity of the dry material (σ_s) was fixed to $5,89.10^{-4}$ S/m and the other parameters were set to c = 1.85 and $d = 3,85.10^{-2}$. The three last parameters were determined by allocating the characteristic values determined for a loamy sand [59]. We assumed that the petrophysical relationship used to derive the volumetric moisture (θ) from the relative dielectric permittivity (ε_r) remains valid for road conditions. We considered a constant antenna height (h_0) equal to 0.49 m for the emitting and receiving antennas, which is quite representative of real applications. The antennas were modeled using 8 point sources and receivers evenly distributed along a horizontal line located at 7.5 cm inward from the antenna aperture. To create synthetic but realistic signals, we simulated radar data with Eq. (4) considering actual antenna properties. Simulations were run for the various configurations using 53 frequencies evenly sampled in a frequency range varying between 490 MHz and 3100 MHz. In these numerical experiments, we assumed frequency-independent dielectric permittivities. However, it is worth noting that, in this operating frequency range, road materials can exhibit dispersive properties arising from water relaxation mechanisms. Despite being neglected in simulations, these effects could be taken into account to get a more realistic wave propagation model when the pavement is significantly wet (e.g., as in [46]).

All signals were then inverted using the SCR and FWI approaches. The first inversion method was carried out in blind test by using the procedure usually applied by the Belgian Road Research Center (BRRC). A file containing 201 comparative calibration traces which were sampled with 1024 points was created to permit the computation of the surface reflection coefficient. We resorted to the peak-to-peak amplitude analysis in the time domain as described in Section 2.1 to achieve this goal. In the case of the bilayered layout, we decided to select a time window ending just after the main peak characterizing the surface reflection in order to retrieve $\varepsilon_{r,1}$. It avoids inversion errors which could arise from the presence of underlying layers. It is particularly useful in cases showing a weak surface permittivity and a strong permittivity contrast between the two first road layers.

Once $\varepsilon_{r,1}$ was known, Eq. (1) was used to estimate the thickness of the first layer. It required the knowledge of the travel time t_1 occurring between the surface and the interface between the two first layers. However, the identification of the interface between the first and the second layer can be hidden by the surface reflection. Therefore, the first step consisted in filtering out the direct wave using the strategy described in Section 2.1. Due to the errors inherent to the method, the reflection peak accounting for the interface between the two layers does not always correspond to

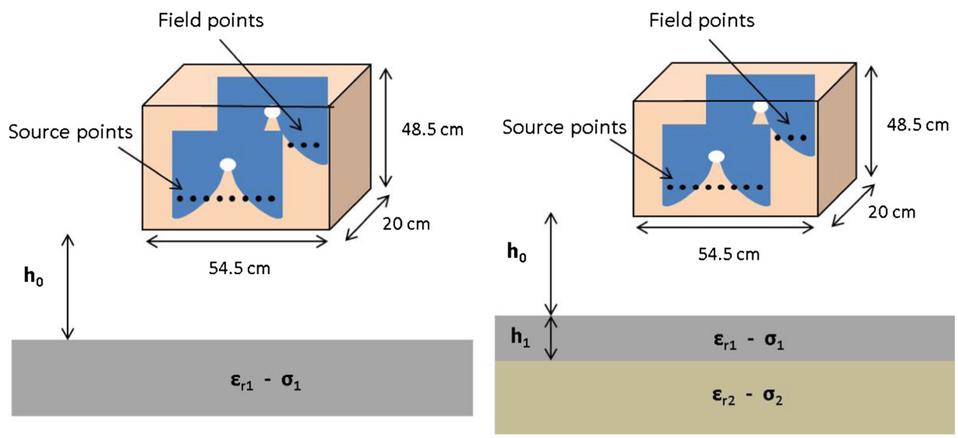

Fig. 4. Monolayer and bilayer layouts used in the numerical experiments.

the absolute maximum of the resulting signal. Knowing that, two assumptions were formulated to improve the detection of interfaces. First, the part of the signal located before or too close to the direct wave was excluded from the investigation domain. It means that, during the second layer detection, we considered only the part of the signal appearing after the main peak accounting for the surface reflection and located at more than the peak-to-peak distance. The peak-to-peak distance is estimated based on the calibration file and is defined as the distance separating the main positive peak from the negative peak preceding it. Second, in order to automate the peak selection procedure, we subtracted from the original signal two identical signals shifted forward and backward by the peak-to-peak distance. The peaks that are preceded or followed by important negative peaks are therefore amplified. The methodology described in Section 2.1 was subsequently used to estimate the permittivity of the underlying layer. We assumed an electrical conductivity equal to 10^{-3} S/m. This value of electrical conductivity is assumed to be reasonable for most of the road materials when these ones are dry.

Once the operations dedicated to the estimation of the parameters were achieved for each synthetic signal, the retrieved parameters were compared to the synthetic ones through the root mean square percentage error (RMSPE). This indicator, which is not affected by the units of the variables, is described in Eq. (13), where $P_{synth,i}$ and $P_{mod,i}$ are the synthetic and retrieved parameter values, respectively, and L is the total number of signals.

$$RMSPE = \sqrt{\frac{1}{L}\sum_{i=1}^{L}\left(100\left|\frac{P_{synth,i} - P_{mod,i}}{P_{synth,i}}\right|\right)^2} \quad (13)$$

We also analyzed the performance of the FWI methodology by resorting to the inverse crime testing procedure and the optimization strategy mentioned in Section 2.2.2. We considered the antenna height as known because it could be determined independently using other methods such as laser measurements. With respect to the monolayer layout, we attempted to retrieve the values of $\varepsilon_{r,1}$ and σ_1 whereas, regarding the second layout, the parameters $\varepsilon_{r,1}$, h_1, σ_1 and $\varepsilon_{r,2}$ were estimated. The electrical conductivity of the bottom layer (σ_2) was set to 0 S/m. Although this electrical conductivity can be significant and frequency-dependent, the influence of this parameter on the signal is negligible in that frequency range as only the permittivity contrast greatly influences the second interface amplitude and there are no deeper interfaces to backscatter the signal propagating in the lower halfspace (see [53]). An important number of parameters implies an important number of iterations during the optimization procedure (±5000), and therefore, an intensive computation time for each signal inversion (several minutes to several hours depending on the number of parameters to retrieve). To address this issue, we elaborated a lookup table (LUT), i.e., a matrix in which signals precomputed for different parameter combinations are stored. We simulated the signals for all combinations of values belonging to the following ranges: $\varepsilon_{r,1} = [3.0 : 0.5 : 13.0], h_1 = [0.010 : 0.005 : 0.100]$ m, $\log_{10}(\sigma_1) = [-3.0 : 0.1 : -1.0]$ S/m and $\varepsilon_{r,2} = [3.0 : 0.5 : 20.0]$. This step took time (several days) but enabled us to avoid performing more time-consuming inversions as, once the LUT is computed, it just has to be read. The computation time devoted to the LUT creation depends on the number of parameters to estimate and the discretization of the parameter spaces. The synthetic measured signal was subsequently compared to those saved in the LUT. The combination of parameters minimizing the error between both was then selected. Afterwards, we compared the retrieved parameters with the theoretical ones and determined the RMSPE value for each parameter. The optimization strategy presented in Section 2.2.2 (combination of GMCS with NMS) was also applied to assess the impact of adding the conductivity of the second layer as an unknown. The parameter spaces investigated were defined in accordance with the ranges used in LUT computations. It is worth noting that the parameter space of σ_2 was identical to the one considered for σ_1. The results of what we call classical full-wave inversions were subsequently compared to the results obtained using the two other methodologies. As the optimization strategy takes significant time, only four signals were subject to this operation.

3.2. Results

Fig. 5 shows the relative permittivity values estimated for both SRC and FWI methods in the case of the monolayer configurations.

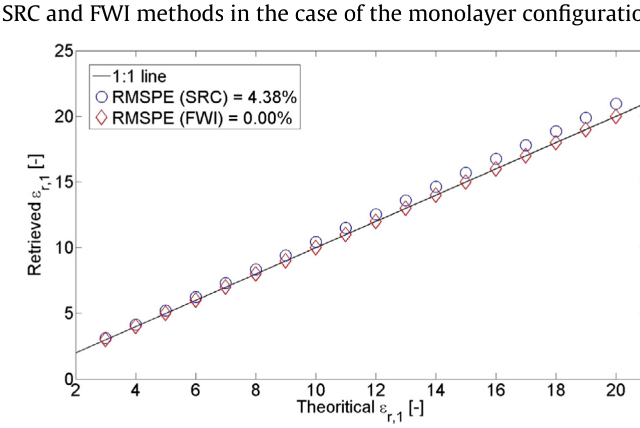

Fig. 5. Comparison between the estimated and simulated $\varepsilon_{r,1}$ resulting from the FWI and the SRC methods for the monolayer layout.

The first methodology gives satisfying estimations of the relative permittivity. The RMSPE, which reaches 4.38%, is consistent with the values referred to in the literature. Fig. 5 highlights that the relative permittivity assessed with this approach is always overestimated. It also evidences that the overestimation increases with the rise of the parameter. It seems to be logical as the sensitivity of the reflection coefficient becomes weaker with the increase of the relative permittivity value. It is worth mentioning that the error associated to this parameter could probably be diminished by taking the angle of incidence into account. Fig. 5 also shows that the FWI approach enabled us to retrieve the exact permittivity values (RMSPE = 0) for all synthetic signals. The electrical conductivity of the medium is also perfectly retrieved even if the sensitivity related to this parameter is weak (not shown here). The restricted number of parameters to estimate, the robust optimization strategy and the inverse crime procedure are the reasons explaining its ability to find the unique global minimum in all inversions.

The same kind of analysis was conducted for the parameters characterizing the bilayer configurations. The results comparing the inverted and theoretical parameter values are shown in Fig. 6. A substantial number of points deviate from the 1:1 line when the SRC method is employed. This mitigated result arises

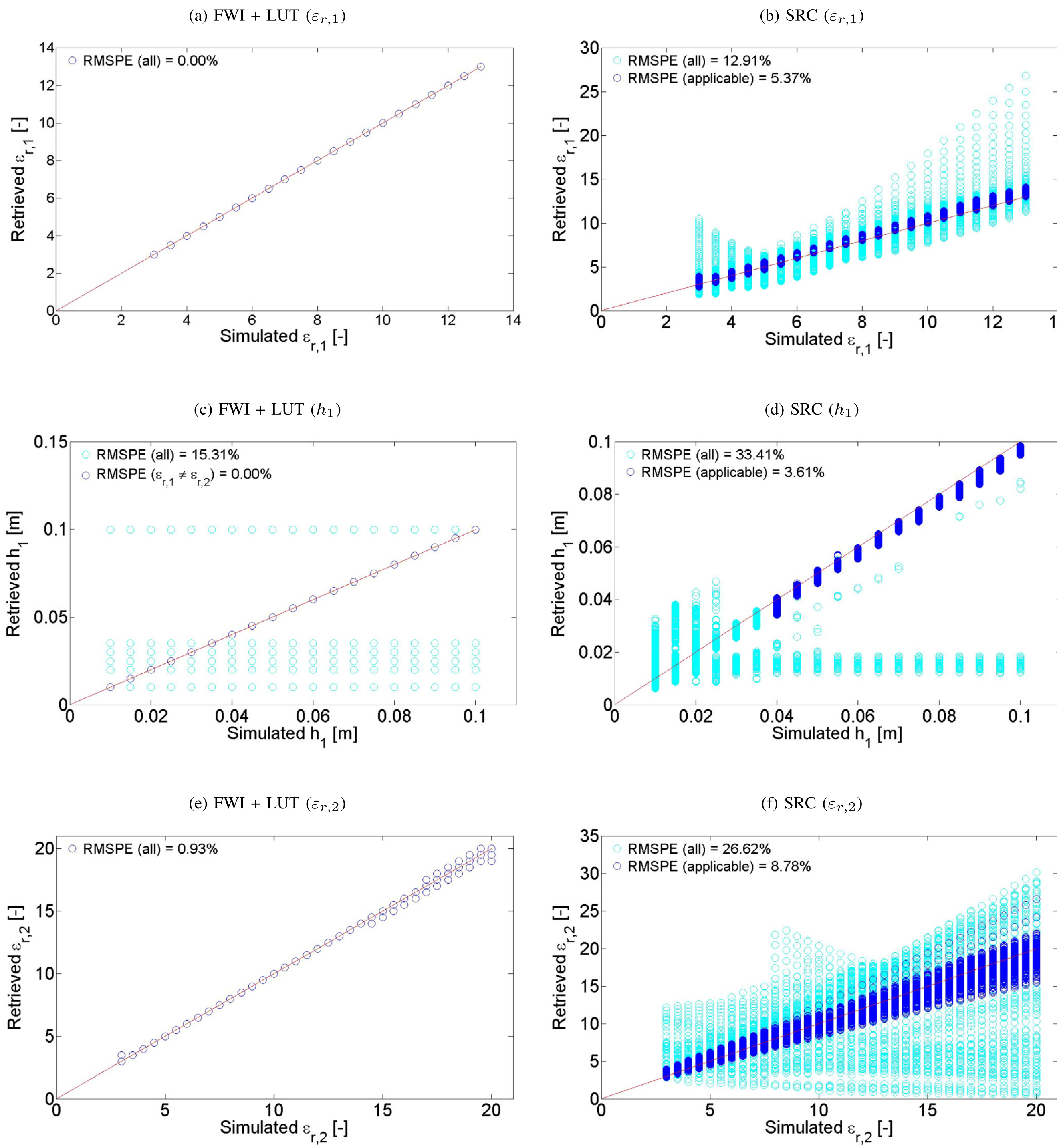

Fig. 6. Comparison between the estimated and simulated $\varepsilon_{r,1}$, h_1 and $\varepsilon_{r,2}$ resulting from the FWI (a, c, e) and SRC methods (b, d, f) for the bilayer layout.

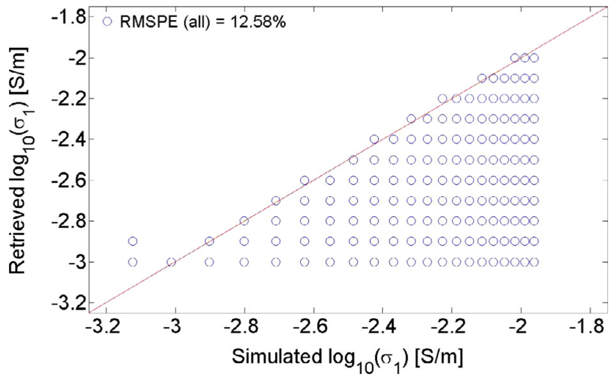

Fig. 7. Comparison between the estimated and simulated σ_1 resulting from the FWI method for the bilayer layout.

from the fact that we considered some cases which are not part of the field of applicability peculiar to the method. Considering a center frequency of 2 GHz and the minimum relative permittivity of the first layer, half the wavelength is slightly larger than 4 cm. If the scenarios with a thin upper layer ($\leqslant$4 cm) are excluded, only cases presenting discrimination between the first and second interface are taken into account. Another limitation inherent to the SRC approach comes from the weak permittivity contrast between the two materials. It also prevents an easy identification of the reflection accounting for the interface between the two media. Omitting these scenarios $\left(\left|\frac{\varepsilon_{r,1}}{\varepsilon_{r,2}}\right| \notin \left[\frac{1}{1.25}, 1.25\right]\right)$ in addition to thin layer cases decreases the RMSPE values associated to $\varepsilon_{r,1}, h_1$ and $\varepsilon_{r,2}$ to 5.37%, 3.61% and 8.78%, respectively. The errors have values that better corresponds to the method performances. Using an expression relating the conductivity to the relative permittivity and considering the frequency dependence of the electromagnetic properties could further improve the results since the materials with a high permittivity are generally more conductive. Fig. 7.

The combination of the FWI approach with the LUT principle allowed providing an estimation of the electrical conductivity of the materials. However, this variable is not easy to estimate as revealed by the high RMSPE value (more than 12%). The inversion strategy tends to underestimate this variable. The conductivity deviation can be substantial regarding scenarios presenting relatively high conductivity values (not shown here). The underestimation could be partly due to the assumption associated to the conductivity of the second layer. This parameter was set to 0 S/m to remove one parameter and thereby limit the computation time dedicated to the LUT. However, in simulated data, this parameter can reach values higher than 0.01 S/m. It leads to perceptible conductivity contrasts which influence the amplitude of the reflections. Therefore, implementing the theoretical σ_1 and $\varepsilon_{r,2}$ values do not necessarily give the best fit between theoretical and modeled data. Nonetheless, it did not prevent us to retrieve accurate values for the other parameters. Fig. 6 shows that the errors associated to the relative permittivities are really low for the FWI approach. The fact that the parameters values used to create the synthetic signals are among those explored with LUT is an additional factor ensuring a better global retrieval of the theoretical parameter values. It is worth noting that conducting the same experiment on a real dataset would increase the error associated to the FWI approach as the antenna transfer functions would have been numerically computed. Despite this favorable factor, the RMSPE associated to the thickness of the first layer slightly exceeds 15%. These discrepancies refer quite logically to cases for which the relative permittivities of the two layers are identical. Excluding these scenarios leads to a RMSPE value equal to 0%. The errors associated to the other parameters $(\varepsilon_{r,1}, \varepsilon_{r,2})$ were not really affected by this operation. These parameters present RMSPE values inferior to 1%.

The results related to the classical parameter optimization are available in Table 1. It shows that the optimization procedure gives an accurate estimation for each of the parameters. Except for the second investigated scenario, the retrieved σ_1 values are closer to the synthetic values than those computed using the lookup table. This statement is quite logical since all combinations of parameters can be tested. More iterations would be necessary to slightly improve the results obtained for the 2^{nd} tested A-scan. Accurate results were also obtained with the SRC method for the four tested scenarios. The thickness of the layer is well estimated although the estimations of σ_1 and σ_2 were neglected.

Both FWI and SRC methods demonstrated a great ability in estimating the required parameters. The field of applicability related to the first approach is wider if the number of layers is a priori known as it enables to model the contribution of interfaces close from each other. Nonetheless, the number of parameters that can be estimated is limited because, as previously mentioned, the classical full-wave inversion is time-consuming. Approximately 50 min were needed to perform about 4000 iterations and retrieve the 5 parameter values characterizing one A-scan. If we increase the number of parameters, and consequently the number of iterations, the computation time related to this method can even be higher. Conversely, about 7 s were sufficient to apply the LUT principle and get accurate results for the same signal. Even though the

Table 1
Comparison of the numerical results provided by the different methodologies for the four selected A-scans.

	Theoritical values				Classical FWI inversion			
Scenario	1	2	3	4	1	2	3	4
$\varepsilon_{r,1}$ [−]	5.00	7.00	8.00	9.00	5.00	7.01	8.00	9.00
h_1 [m]	0.04	0.09	0.06	0.05	0.04	0.09	0.06	0.05
$log_{10}(\sigma_1)$ [S/m]	−2.71	−2.42	−2.32	−2.23	−2.71	−2.66	−2.32	−2.23
$\varepsilon_{r,2}$ [−]	8.00	12.00	16.50	12.50	8.00	11.87	16.50	12.50
$log_{10}(\sigma_2)$ [S/m]	−2.32	−2.02	−1.80	−1.99	−2.32	−2.32	−1.80	−1.99
	FWI + LUT inversion				SRC inversion			
Scenario	1	2	3	4	1	2	3	4
$\varepsilon_{r,1}$ [−]	5.00	7.00	8.00	9.00	5.03	7.27	8.44	9.51
h_1 [m]	0.04	0.09	0.06	0.05	0.039	0.088	0.058	0.05
$log_{10}(\sigma_1)$ [S/m]	−3.00	−2.50	−3.00	−2.40	–	–	–	–
$\varepsilon_{r,2}$ [−]	8.00	12.00	16.00	12.50	8.35	12.78	15.53	12.22
$log_{10}(\sigma_2)$ [S/m]	–	–	–	–	–	–	–	–

second strategy allows us to estimate these variables with a reasonable computation time, the LUT has to be calculated in advance once and for all. In this study, about 2 days were dedicated to achieve this step and provide simulated radar signals with sufficiently detailed ranges of values for $\varepsilon_{r,1}, h_1, \sigma_1$ and $\varepsilon_{r,2}$ (Intel Core CPU 3.40 GHz, Matlab environment). Adding more parameters or defining a finer sampling of the parameter spaces would proportionally increase the computation time. However, the lengthy computation time does not represent a real issue nowadays because several strategies aiming at limiting burdening calculations are available. The optimization of the number of frequencies required to solve a particular inverse problem is a first option. De Coster et al. [61] showed that a reasonable decrease of the number of frequencies may not affect the reconstruction of multilayered media. Information content analyses can be used to help determining the appropriate number of frequencies. To resort to clusters and a parallelization procedure would be a second solution to drastically reduce the LUT creation time as calculations could be conducted independently for each precomputed signal. It is worth noting that, in contrast to computation time, the nonuniqueness and the instability of the inverse solution are real issues. For its part, the surface reflection coefficient method is much faster as about 10 s were needed to provide an estimation of the parameters for the whole set of signals processed in blind test conditions. However, under specific conditions, the errors associated to the retrieval of the parameters can sometimes be quite important. As shown through the multilayered scenario, the presence of a thin layer can lead to constructive or destructive interferences and, hence, to larger or smaller reflections. These interferences are neglected in the SRC methodology whereas they are, to some extent, included in the FWI approach. The results nonetheless demonstrated the good performances of the SRC approach when its field of applicability is respected. Taking into account the antenna geometry (reflection angle) and calculating the surface reflection coefficient in the frequency domain could potentially further enhance these results.

4. Laboratory experiments

The laboratory experiment permits to go one step further as the noise and heterogeneities inherent to real-case surveys are taken into account.

4.1. Test site description and data acquisition

Measurements were carried out in the Belgian Road Research Centre (BRRC) facilities of Wavre. The test site (Fig. 8) is an area composed of eight sections of 2.7 m wide distributed over a 23 m long profile. Four of these Sections 1–4 are pavement structures that can be typically encountered in Belgium. Zones 1 and 2 are characterized by two asphalt layers covering concrete and lean concrete, respectively, whereas zone 3 consists of an asphalt layer covering cobblestones. Zone 4 is for its part made up of a concrete layer separated from a lean concrete layer by a thin asphalt layer. The four other sections (a, b, c and d) are in fact transitions areas which were required to build the road structures previously described. The road formation and the base layer are composed of local silty soil and recycled concrete aggregates, respectively. Some utilities (dowels, temperature sensors and strain gauges of about 10 cm long) were deliberately buried in zones a, c and d. A void under a concrete slab was reproduced in zone 1 while an artificial slope and an adherence default between two bituminous layers were simulated in zone c.

The thickness of the pavement layers were controlled throughout the construction phase using topographic measurements. The nominal thickness and the thickness measured using topographic methods are summarized in [62]. The cumulated thickness of the two asphalt layers located in zones 1 and 2 is slightly (5–6 mm) lower than thickness initially planned (10 cm). The measurements performed at the top and at the bottom of the concrete plates in zone 1 show that its thickness is higher than the nominal value (20 cm) and varies from 20.1 cm close to the cobblestones to 21.8 cm close to the lean concrete. The topographic measurements conducted at the base of the thin asphalt layer in zone 4 evidence that the total thickness of the upper materials differs from the expected value by 1.7 cm (24.3 cm instead of 26 cm). The discrepancies observed between the expected and measured values can arise from a lack of accuracy during the construction.

A dataset was acquired along a 26.79 m long transect using a time domain radar system. The radar system, which was composed of a SIR-20 control unit connected to a 2 GHz air-coupled GSSI horn antenna, was suspended at the back of a van at approximatively 0.47 m above the pavement surface. The back wheel of the vehicle was equipped with an odometer to accurately determine the travelled distance and trigger GPR measurements at defined intervals (sampling density equal to 100 scans/m) [63].

4.2. Data processing and inversions

Some processing steps were performed prior to the determination of the properties of the pavement layers. We began by applying high-pass and low-pass frequency filters to the data acquired along the profile. The frequency range was limited between 0.9 GHz and 3.6 GHz in which 54 frequencies were sampled. A noise reduction filter provided by GSSI and an automatic picking

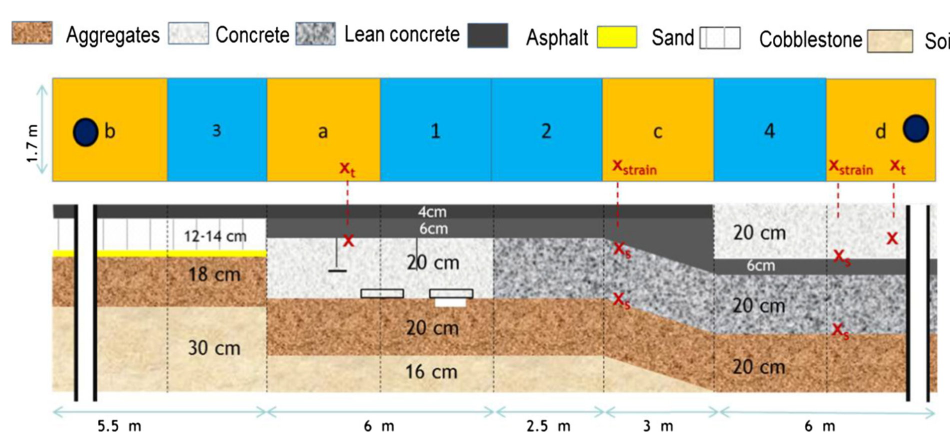

Fig. 8. Configuration of the Belgian Road Research Centre test site (Wavre, Belgium) used in laboratory experiments [62].

procedure able to detect layers and buried structures were also used as preliminary steps of the surface reflection coefficient (SRC) approach. Before conducting the survey, calibration measurements were performed over a perfect reflector directly placed on the ground in zone d. In the full-wave inversion (FWI) approach, the calibration procedure aiming at computing the antenna characteristic coefficient functions was *a posteriori* achieved in the Hydrogeophysics laboratory of the Université catholique de Louvain (Belgium) according to the procedure referred in details in Lambot and André [51]. We decided to restrict the calibration to antenna heights varying from 0.25 m to 0.70 m. It permitted to minimize errors in the retrieved antenna transfer functions while covering the antenna heights generally used by road administration agencies.

The FWI methodology requires an additional processing step because, as shown in Fig. 9, the removal of the free-space antenna response (H_i) from the data does not give satisfying results for time domain radar systems. As shown in a previous study (Mahmoudzadeh and Lambot [63]), time domain systems appear to be less stable and less repeatable than frequency domain systems, which affects the calibration and inversion performances. The radar source instability tends to create a drift in the propagation time of the signal as well as a variation of the signal in terms of amplitude. These problems can be explained by the jitter, i.e., the uncertain sampling time interval of the received signal. In that respect, we developed a correction procedure to take into account the radar source instability. The correction ensures an adapted antenna effects removal and a proper signal inversion procedure through the model described in Section 2.2.1. The correction procedure involves several steps: (1) to identify in the measured signal a zero-crossing propagation time (t_{cross}) situated between the antenna internal reflections arrival time and the surface reflection arrival time, (2) to set in the time domain the part of the measured signal and the part of the free-space antenna response beyond t_{cross} to zero, (3) to derive the correction factor f_c by dividing in the frequency domain the time-limited measured signal $S_t(\omega)$ by the time-limited free-space antenna response $H_{it}(\omega)$ (See Eq. (14)) and (4) to divide in the frequency domain the initial measurement $S(\omega)$ by the correction factor to obtain the corrected signal $S_c(\omega)$ (See Eq. (15)). It is worth noting that this operation is relevant only if the medium surface can be discriminated from the antenna internal reflections.

$$f_c = \frac{S_t(\omega)}{H_{it}(\omega)} \tag{14}$$

$$S_c(\omega) = \frac{S(\omega)}{f_c} \tag{15}$$

Finally, we used the surface reflection coefficient (SRC) and the full-wave inversion (FWI) methods described in Sections 2.1 and 2.2, respectively, in order to estimate the thickness and relative

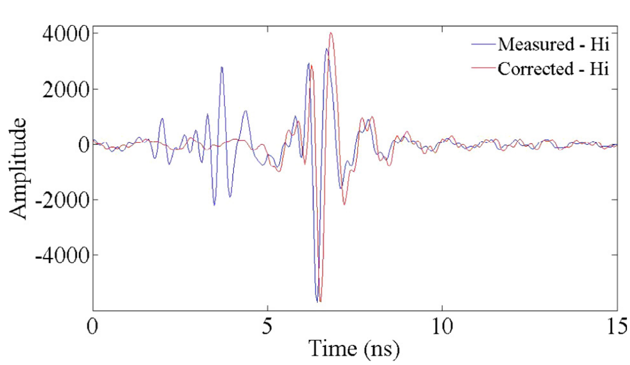

Fig. 9. Impact of the correction procedure on the H_i transfer function removal.

permittivity of the materials. Before anything else, we restricted the area under investigation to zones 1 and 2 for several reasons. First, these areas do not contain any scattering object that could affect the inversion results (in opposition to transition areas). Secondly, the interface between the asphalt and cobblestones in zone 3 is assumed to be rough, which makes difficult the validation of the retrieved thickness. Finally, we omitted zone 4 because the conductivity of the layers are neglected during parameter optimization whereas the first layer is composed of concrete and is therefore subject to attenuation processes.

In both SRC and FWI approaches, we split the problem into two stages. In the first stage, we focused inversions on the surface reflection in order to get a first estimation of the antenna height (h_0) (for FWI only) and the relative permittivity of the first layer ($\varepsilon_{r,1}$) at every position. Then, during the second stage, we conducted a second set of inversions to estimate the thickness of the first layer (h_1) and the permittivity of the second layer ($\varepsilon_{r,2}$) (for FWI only) as additional unknowns. We restricted the time window to the propagation time of the first layer reflection to avoid the influence of the underlying layers on results. Regarding the FWI approach, the parameter spaces implemented in the optimization procedure were constrained in order to reduce the complexity of the inverse problem. It limits the probability that the sequential combination of algorithms (GMCS + NMS) leads to a local minimum and, thereby, to wrong parameter values. The following ranges of parameter values were employed in final inversions: h_0 = [0.53 …0.57] m, $\varepsilon_{r,1}$ = [2 …8], h_1 = [0.02 …0.08] m and $\varepsilon_{r,2}$ = [2 …8]. To avoid a computationally burdening inversions, we assumed a fixed conductivity value equal to 10^{-4} S/m and 0 S/m for the first and second layer, respectively.

4.3. Results and discussion

Fig. 10 shows the image of the GPR data acquired along the test site after applying a gain function. The analysis of the GPR data allows identifying quite clearly the major part of the surface and underground structures/utilities. The air-pavement interface leads to the strong reflection appearing at about 6.5 ns. The two investigation chambers are detected at the same propagation time and are located at x = 0.9 m and x = 22 m, respectively. The GPR image also permits to spot the bottom of the cobblestones, two strain gauges ([x, t] = [2.48 m, 3.56 ns] and [23,48 m, 3.52 ns]), the void located in zone 1 ([x, t] = [11.3 m, 9.00 ns]) and some layers of the pavement structures. The interface between the asphalt and the concrete in zones 1 and 2 as well as the interface between the lean concrete and the aggregates in zone 2 are in particular identified. Although its reflection remains weak, we are able to discriminate with difficulty the boundary between the aggregates and the silty soil in zone 2.

We also resorted to the physically-based modeling approach described in Section 2.2.1 to filter out the antenna multiple reflections and the antenna-medium ringing from raw GPR data. As the measurements were acquired at heights close from far-field conditions, we decided to reduce the number of point sources and field points to one, which reduces the generalized model to the far-field model proposed by Lambot et al. [46]. Fig. 11 shows the corresponding time domain radar image after having filtered out antenna effects. Several improvements can be noticed compared to the unfiltered GPR image. First, the antenna internal reflections and the antenna-medium multiple reflections are efficiently removed from the data. Secondly, the surface reflection has been time-shifted and the time zero corresponds now to the antenna phase center. The propagation times are not affected by antenna distortions and permit to determine more accurately the depth of the objects from the straight ray propagation times. Third, we

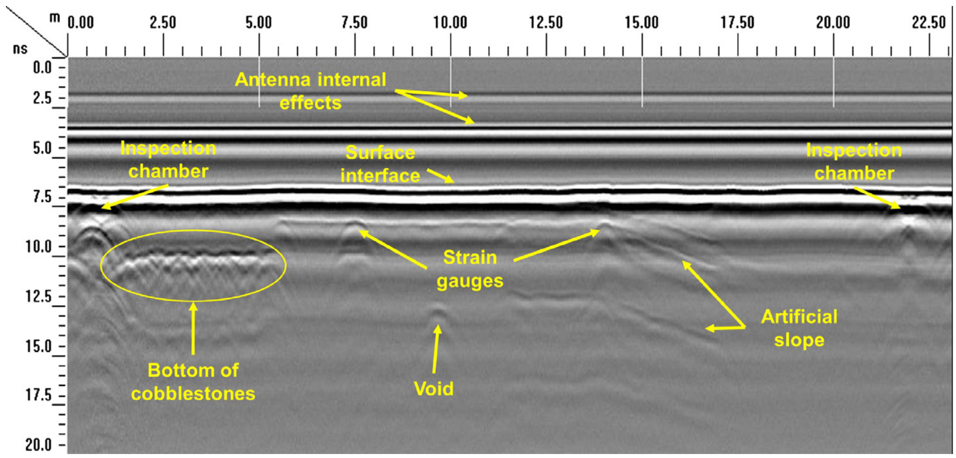

Fig. 10. GPR data acquired along the BRRC test site with the time domain radar system.

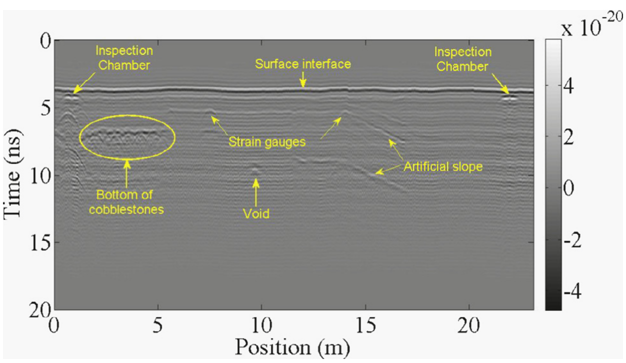

Fig. 11. GPR data acquired along the BRRC test site with the time domain radar system after applying the antenna effects removal approach.

observe an enhancement in terms of resolution which is illustrated, e.g., by the fact that we clearly discriminate the inspection chamber reflections from the road surface reflection. A slight spectral leakage effect is nonetheless noticed in the filtered image. It results from the inverse Fourier transform and the limited frequency range. This artefact makes the interface between the aggregates and the silty soil impossible to detect.

Fig. 12a shows the antenna height profile retrieved for zones 1 and 2 using full-wave inversions. The antenna height varies from 0.482 m to 0.494 m. These values are slightly lower than the value measured during data acquisition. The difference could be caused by errors in the measurement and/or the calibration procedure (e.g., inclination of the box containing the antennas). The variation of the antenna height along the profile is partly explained by the changes of the vehicle speed. Fig. 12b compares the surface relative permittivity values retrieved for zones 1 and 2 using the FWI (blue) and SRC (red) methods. The relative permittivity of the surface layer is slightly oscillating between 2.92 and 4.60 for the FWI approach whereas it ranges between 4.02 and 4.92 for the SRC approach. The average value calculated for this electromagnetic property is about 3.90 and 4.49 for FWI and SRC approaches, respectively. It is worth noting that both methods show $\varepsilon_{r,1}$ profiles having a constant general trend even if a slight decrease of the relative permittivity is observed between $x = 11$ m and $x = 12.8$ m with the FWI approach. The origin of the differences observed with the two methods is to be attributed to the fact that with the FWI approach, antenna effects are accounted for whereas they are still part of the data that are processed with the SRC approach. Fig. 12b also shows that the permittivity values estimated using full-wave inversions are always lower than those computed with the surface reflection coefficient approach. These differences mainly arise from the correction procedure used in the FWI approach. The correction, which aims at taking into account the radar source instability, seems to affect the surface reflection originally recorded. A small part of the discrepancies between the two characterization methods is also attributed to the slightly different choice regarding the maximal time window considered during the estimation of the parameters. Although the values retrieved using FWI appear quite weak in some part of the profile, the results of the two methods are in agreement with the range of relative permittivities considered for such material.

Fig. 12c compared the thickness of the first asphalt layer retrieved for zones 1 and 2 using FWI and SRC methods. We restricted the inversions to the first centimeters of the multilayered medium in order to limit the influence of deeper layers on h_1 estimates. The thickness ranges between 0.033 m and 0.061 m for the SRC approach with an average value equal to 0.044 m whereas it ranges between 0.024 m and 0.065 m for the FWI approach with an average value equal to 0.044 m. It is worth noting that the values estimated for the parameters never reached the parameter space boundaries during the optimization procedure. Most of h_1 values estimated using the SRC method are centered around 4.5 cm even if we observe some outliers. The outliers can partly be explained by the fact that the conditions required to ensure an automatic detection of h_1 are not properly respected (quite thin asphalt layer and small permittivity contrast). The strong variation of thickness observed between 11.5 m and 13.0 m can partly be attributed to the presence of a transition area (zone c). Fig. 12c shows that the thickness values estimated using full-wave inversions are split into two groups of values. The thickness values retrieved for positions located between 8.0 m and 9.0 m as well as 9.8 m and 11.2 m are centered around 2.75 cm although some punctual estimates give higher values. The thickness values estimated between 9.0 m and 9.8 m fluctuate between 4.5 cm and 5.0 cm. FWI results also evidence a gradual rise of h_1 from 5.0 cm to more than 6.0 cm for the signals acquired between 11.2 m and 12.7 m. These high values of thickness result from the decrease of $\varepsilon_{r,1}$ observed in Fig. 12b. The presence and detection of a slanting located in zone c could explain this decrease in relative permittivity. Finally, Fig. 12d shows the relative permittivity of the second asphalt layer retrieved using FWI along the same area. The value computed for this parameter oscillates between 2.67 and 5.92, with a average value equal to 4.01. The results highlight that the permittivity of the two asphalt layers are really close to each other.

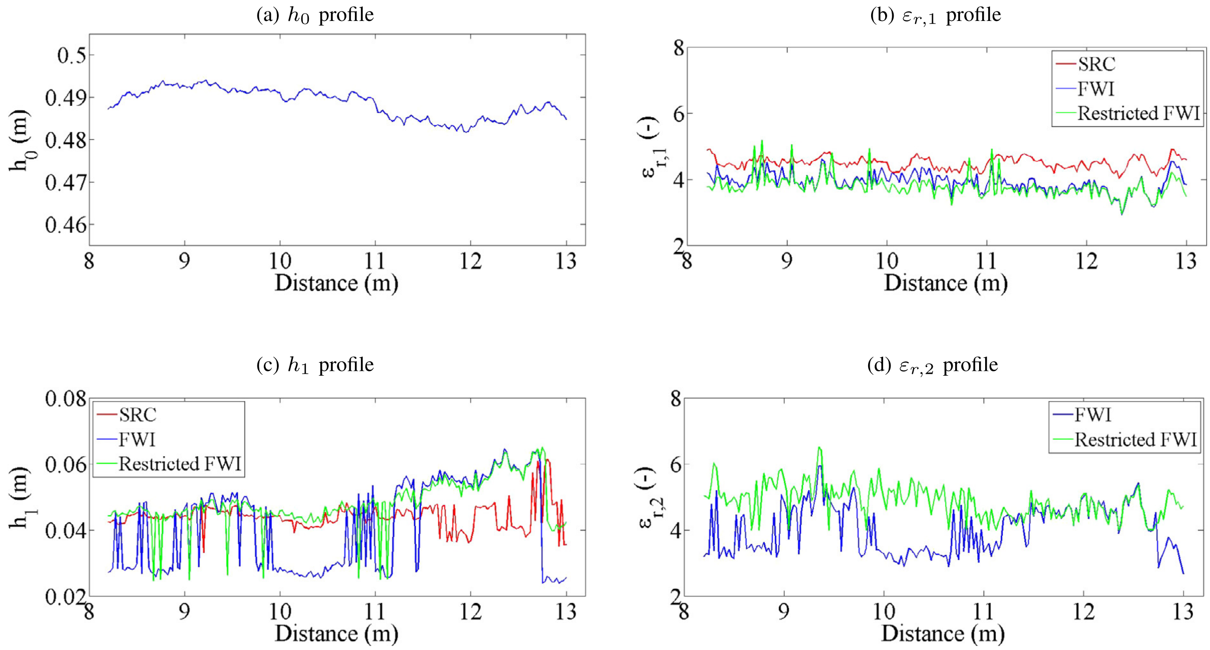

Fig. 12. (a) h_0, (b) $\varepsilon_{r,1}$ (c) h_1 and (d) $\varepsilon_{r,2}$ values retrieved using the SRC and FWI approaches along zones 1 and 2.

The high variability of the thickness retrieved with the FWI approach is partly attributed to the low electromagnetic contrast existing between the two asphalt layers. The absence of a clear reflection makes the automatic identification of the interface difficult to achieve, which prevents the algorithms to accurately estimate the parameter values. To understand the differences existing within the values of thickness retrieved through inversions, we computed the 2-D response surface topographies of the objective functions for the signals acquired at the positions x = 10 m (low thickness value) and x = 12 m (high thickness value). The objective functions pertaining to the cases with low and high thickness values are presented in Fig. 13. To better highlight their topographies, the objective function values are expressed in a logarithmic scale. It is worth noting that h_0 and $\varepsilon_{r,1}$ values, which were beforehand retrieved through full-wave inversions, were implemented as input to compute the values of the objective functions.

The objective function topography related to the position x = 10 m (Fig. 13a) shows that 2 minima are enclosed in a long blue valley which evidences a quite poor sensitivity with respect to the layer thickness. Nonetheless, the results highlight that the parameter values retrieved by inversion correspond to those permitting to minimize the objective function. The sequential combination of GMCS and NMS therefore succeeded in finding the global minimum. The objective function topography related to the position x = 12 m (Fig. 13b) shows a more oscillating behavior and the presence of numerous local minima. The global minimum shows, however, an error value substantially lower than those computed for the other minima. The combination of the parameters minimizing the objective function corresponds to the one retrieved through the response surface topography analysis. Nevertheless, the h_1 and $\varepsilon_{r,2}$ values minimizing the function at x = 10 m and x = 12 m are not the same for the two signals. Although the algorithm nearly always finds the global minimum of the objective function, this one does not necessarily appear at the right place (for the correct combination of parameters). In fact, the place of the global minimum changes depending on the measurement and modeling errors. In our case, the relatively flat topography of the objective functions allows the position of the global minimum to be considerably displaced, even if it is discontinuously (local minima have similar depth than the global one). We therefore face up to an instability of the inverse solution. The lack of information (low contrast) is an hypothesis that can be put forth to explain the instability issue.

As shown in Fig. 12d, the relative permittivity values retrieved for the second layer $\varepsilon_{r,2}$ are close to 3 when the thickness values

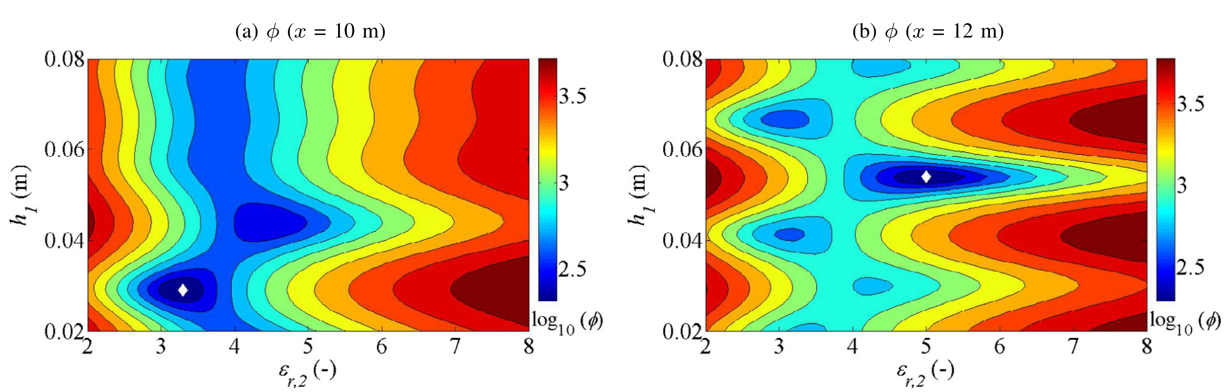

Fig. 13. 2-D response surfaces of the objective functions for the signal acquired at (a) 10 m and (b) 12 m from the beginning of the transect.

h_1 are low. A relative permittivity value of 3 seems to be weak for an asphalt layer. Therefore, in order to avoid non-physical solutions, we have reason to restrict the parametric space while remaining relatively general with regard to real applications. We decided to restrict the lower boundary of this parameter to 4 in the optimization procedure. This operation is likely to prevent the local minima to become global further to measurement and modeling errors. The values of $\varepsilon_{r,1}, h_1$ and $\varepsilon_{r,2}$ resulting from these new full-wave inversions are shown in Fig. 12b, c and d, respectively (green curves). We observe that the $\varepsilon_{r,1}$ profile is quite similar to the one estimated without restricting the parameter space even if few peaks of high value are noticed. The $\varepsilon_{r,1}$ profile oscillates between 2.97 and 5.18 with an average value equal to 3.77.

The results regarding h_1 (Fig. 12c) shows that the value of this parameter is relatively constant around 4.5 cm between 8.0 m and 11.0 m. Regarding these positions, the thickness profile is therefore similar to the one retrieved using the SRC method. We notice that the positions of the thickness estimates showing values lower than 3.0 cm correspond to the positions where we observe $\varepsilon_{r,1}$ peaks. In fact, the increase of $\varepsilon_{r,1}$ leads to a decrease of the wave velocity. Therefore, h_1 has also to decrease in order to keep an identical interface reflection arrival time. These specific outliers result from optimization issues. After $x = 11$ m, the thickness curve progressively increases until reaching 6.5 cm at a distance equal to 12.8 m for the reasons that were previously described. This trend is not observed in the thickness profile computed based on the SRC approach. In this area, the SRC results shows values that are inconsistently distributed between 3 cm and 6 cm. The FWI approach also shows an important drop of the thickness occurring at $x = 12.8$ m. It corresponds to the position at which the asphalt-asphalt interface reflection stopped to be affected by the slanting reflection present in the transition area. Aside from these discrepancies, both SRC and FWI methods give similar thickness profiles with values generally close to the expected thickness value (4 cm).

5. Summary and conclusion

In this study, we propose to numerically and experimentally analyze the capabilities of the surface reflection coefficient and full-wave inversion methods to estimate the electromagnetic and physical properties of pavements. The numerical experiments were carried out in blind test for the SRC approach whereas FWI was subject to an inverse crime testing procedure. The SRC results show that the root mean square percentage errors associated to the estimation of the thickness of the first layer, the relative permittivity of the first layer and the relative permittivity of the second layer are around 3.6%, 5.4% and 8.8%, respectively, when the scenarios are part of the method field of applicability. The FWI results provided through the inverse crime procedure show that the error is inferior to 1% for all parameters. FWI therefore applies to a wider range of configurations but is nonetheless more computation-intensive. A laboratory experiment was also conducted using a time domain radar system in order to study the impact of the noise and heterogeneities inherent to real pavement investigation. The results evidence the importance of adequately processing the data prior to inversions, especially when a radar source instability is observed. The results also show that we face up to an instability of the inverse solution caused by a limited information content. However, with an adaptation of their inversion strategies, both methods provided thickness values which were similar and in accordance with the expected value. Future research will focus on the application of the methods to data acquired with antennas placed closer to the pavement surface and with frequency domain radars.

Acknowledgements

This work was supported and funded by the Walloon Region through the ‘‘SENSPORT” project (Convention n°1217720) undertaken in the framework of the WBGreen research program. All the works completed by the BRRC were undertaken in the framework of the Georadar pre-normalization project, subsidized by the NBN (Belgian Bureau for Normalization). We also benefited from the FNRS-Belgium (Fonds National de la Recherche Scientifique) support and the networking activities carried out within the EU funded COST Action TU1208 ‘‘Civil Engineering Applications of Ground Penetrating Radar”.

References

[1] W. Uddin, An overview of gpr applications for evaluation of pavement thickness and cracking, in: Proceedings of the 15th International Conference on Ground Penetrating Radar, Brussels, Belgium, Jun. 2014, pp. 925–930.
[2] T. De Jonghe, C. De Backer, P. Brichant, Code de bonne pratique pour le choix du revêtement bitumineux lors de la conception ou l'entretien des chaussées, Belgian Road Research Center (BRRC), 2006.
[3] I.L. Al-Qadi, S. Lahouar, Measuring layer thicknesses with GPR – Theory to practice, Constr. Build. Mater. 19 (10) (2005) 763–772.
[4] A. Loulizi, I.L. Al-Qadi, S. Lahouar, Optimization of ground-penetrating radar data to predict layer thicknesses in flexible pavements, J. Trans. Eng. 129 (1) (2003) 93–99.
[5] A. Benedetto, S. Pensa, Indirect diagnosis of pavement structural damages using surface GPR reflection techniques, J. Appl. Geophys. 62 (2) (2007) 107–123.
[6] R.D. Evans, M.W. Frost, M. Stonecliffe-Jones, N. Dixon, A review of pavement assessment using ground penetrating radar (GPR), in: Proceedings of the 12th International Conference on Ground Penetrating Radar), Birmingham, UK, Jun. 2008, pp. 1–10.
[7] H. Von Quintus, C. Rao, R. Minchin, S. Nazarian, K. Maser, B. Prowell, NCHRP Report 626. Transportation Research Board, National Research Council, 2009, ch. NDT technology for quality assurance of HMA pavement construction, p. 112.
[8] G. Clemena, M. Sprinkel, R.J. Long, Use of ground penetrating radar for detecting voids under a jointed concrete pavement, Trans. Res. Rec. J. Trans. Res. Board 1109 (1987) 1–10.
[9] K. Grote, S. Hubbard, J. Harvey, Y. Rubin, Evaluation of infiltration in layered pavements using surface GPR reflection techniques, J. Appl. Geophys. 57 (2) (2005) 129–153.
[10] C. Plati, A. Loizos, Estimation of in-situ density and moisture content in HMA pavements based on GPR trace reflection amplitude using different frequencies, J. Appl. Geophys. 97 (2013) 3–10.
[11] F. Fernandes, J. Pais, Assessment of moisture in road pavements, in: Proceedings of the 15th International Conference on Ground Penetrating Radar, Brussels, Belgium, Jun. 2014, pp. 909–912.
[12] I.L. Al-Qadi, Z. Leng, S. Lahouar, J. Baek, In-place hot-mix asphalt density estimation using ground-penetrating radar, Trans. Res. Rec. J. Trans. Res. Board 2152 (2) (2010) 19–27.
[13] Z. Leng, I.L. Al-Qadi, S. Lahouar, Development and validation for in situ asphalt mixture density prediction models, NDT & E Int. 44 (4) (2011) 369–375.
[14] S. Cardimona, B. Willeford, D. Webb, S. Hickman, J. Wenslick, N. Anderson, Automated pavement analysis in Missouri using ground penetrating radar, in: Proceedings of the 2nd Annual Conference on the Application of Geophysical and NDT Methodologies to Transportation Facilities and Infrastructure, vol. FHWA-WCR-02-001, California, USA, Apr. 2003, pp. 1–10.
[15] A. Benedetto, F. Benedetto, M.R. De Blasiis, G. Giunta, Reliability of signal processing technique for pavement damages detection and classification using ground penetrating radar, IEEE Sens. J. 5 (3) (2005) 471–480.
[16] D. Huston, N. Pelczarki, B. Esser, K. Maser, Damage detection in roadways with ground penetrating radar, in: Proceeding SPIE of the 8th International Conference on Ground Penetrating radar, vol. 4084, Gold Coast, Australia, Apr. 2000, pp. 91–94.
[17] G. Morcous, E. Erdogmus, Accuracy of ground-penetrating radar for concrete pavement thickness measurement, J. Perform. Constr. Facilities 24 (6) (2010) 610–621.
[18] I.L. Al-Qadi, S. Lahouar, Measuring rebar cover depth in rigid pavements with ground-penetrating radar, Trans. Res. Rec. J. Trans. Res. Board 1907 (1) (2005) 81–85.
[19] T. Saarenketo, T. Scullion, Road evaluation with ground penetrating radar, J. Appl. Geophys. 43 (2–4) (2000) 119–138.
[20] A. Loizos, C. Plati, Accuracy of pavement thicknesses estimation using different ground penetrating radar analysis approaches, NDT and E Int. 40 (2) (2007) 147–157.
[21] Z. Leng, I.L. Al-Qadi, An innovative method for measuring pavement dielectric constant using the extended CMP method with two air-coupled GPR systems, NDT and E Int. 66 (2014) 90–98.

[22] C. Guattari, F. Amico, A. Benedetto, Integrated road pavement survey using GPR and LFWD, in: Proceeding of the 13th International Conference on Ground Penetrating radar, Lecce, Italy, Jun. 2010, pp. 1–6.
[23] A. Noureldin, K. Zhu, S. Li, D. Harris, Network pavement evaluation with falling-weight deflectometer and ground-penetrating radar, Trans. Res. Rec. J. Trans. Res. Board 1860 (2003) 90–99.
[24] S. Lahouar, I.L. Al-Qadi, Automatic detection of multiple pavement layers from GPR data, NDT and E Int. 41 (2) (2008) 69–81.
[25] Q. Li, Z. Xia, J. Shao, J. Chen, X. Liu, G. Fang, Non-destructive survey of pavement layer thicknesses with ground penetrating radar, in: TENCON, IEEE Region 10 International Conference, Xi'an, China, Oct. 2013, pp. 1–4.
[26] C. Van Geem, C. Grégoire, Rehabilitation of roads containing cobblestone pavements covered with a bituminous layer, in: Proceedings of the 9th Conference on the Bearin Capacity of Roads, Railways and Airfields, Trondheim, Norway, Jun. 2013, pp. 1–18.
[27] R.D. Evans, M.W. Frost, M. Stonecliffe-Jones, N. Dixon, Assessment of the in-situ dielectric constant of bituminous pavement materials, Trans. Res. Rec. J. Trans. Res. Board 2037 (2007) 128–135.
[28] W. Muller, Self-correcting pavement layer depth estimates using 3D multi-offset ground penetrating radar (GPR), in: Proceedings of the 15th International Conference on Ground Penetrating Radar, Brussels, Belgium, Jun. 2014, pp. 887–892.
[29] D. Wright, V. Baltazart, N. Elsworth, R. Hamrouche, J. Krarup, M. Lurdes Antunes, S. McRobbie, V. Merecos, T. Saarenketo, Monitoring structural and surface conditions, in TRIMM project FP7-285119, no, Delivrable D4 (3) (2014) 160.
[30] C. Fauchard, X. Dérobert, J. Cariou, P. Côte, GPR performances for thickness calibration on road test sites, NDT and E Int. 36 (2) (2003) 67–75.
[31] M. Solla, H. González-Jorge, H. Lorenzo, P. Arias, Uncertainty evaluation of the 1 GHz GPR antenna for the estimation of concrete asphalt thickness, Meas.: J. Int. Meas. Confeder. 46 (9) (2013) 3032–3040.
[32] T. Scullion, C. Lau, Y. Chen, Pavement evaluation using ground penetrating radar in Texas, in: Proceedings of the 5th International Conference on Ground Penetrating Radar, Ontario, Canada, Jun. 1994, pp. 449–463.
[33] I.L. Al-Qadi, S. Lahouar, A. Loulizi, Successful application of ground-penetrating radar for quality assurance quality control of new pavements, Trans. Res. Rec. J. Trans. Res. Board 1861 (2003) 86–97.
[34] S. Zhao, P. Shangguan, I. Al-Qadi, Application of regularized deconvolution technique for predicting pavement thin layer thicknesses from ground penetrating radar data, NDT and E Int. 73 (2015) 1–7.
[35] R. Hamrouche, T. Saarenketo, Improvement of a coreless method to calculate the average dielectric value of the whole asphalt layer of a road pavement, in: Proceddings of the 15th International Conference on Ground Penetrating Radar, Brussels, Belgium, Jun. 2014, pp. 899–902.
[36] S. Lahouar, I.L. Al-Qadi, A. Loulizi, T. Clark, D. Lee, Approach to determining in situ dielectric constant of pavements: development and implementation at interstate 81 in Virginia, Trans. Res. Rec. J. Trans. Res. Board 1806 (1) (2002) 81–87.
[37] C.P. Kao, J. Li, Y. Wang, H. Xing, C.R. Liu, Measurement of layer thickness and permittivity using a new multilayer model from GPR data, IEEE Trans. Geosci. Remote Sens. 45 (8) (2007) 2463–2470.
[38] H. Liu, M. Sato, In situ measurement of pavement thickness and dielectric permittivity by GPR using an antenna array, NDT and E Int. 64 (2014) 65–71.
[39] J. Virieux, S. Operto, An overview of full-waveform inversion in exploration geophysics, Geophysics, vol. 74, no. 6, pp. WCC127–WCC152, Nov. 2009.
[40] A. Kalogeropoulos, J. Van Der Kruk, J. Hugenschmidt, J. Bikowski, E. Brühwiler, Full-waveform GPR inversion to assess chloride gradients in concrete, NDT and E Int. 57 (2013) 74–84.
[41] C. Patriarca, S. Lambot, M.R. Mahmoudzadeh, J. Minet, E. Slob, Reconstruction of sub-wavelength fractures and physical properties of masonry media using full-waveform inversion of proximal penetrating radar, J. Appl. Geophys. 74 (1) (2011) 26–37.
[42] K.Z. Jadoon, S. Lambot, B. Scharnagl, J.V.D. Kruk, E. Slob, H. Vereecken, Quantifying field-scale surface soil water content from proximal GPR signal inversion in the time domain, Near Surface Geophysics 8 (6) (2010) 483–491.
[43] J. Minet, P. Bogaert, M. Vanclooster, S. Lambot, Validation of ground penetrating radar full-waveform inversion for field scale soil moisture mapping, J. Hydrol. 424–425 (2012) 112–123.
[44] G. Gentili, U. Spagnolini, Electromagnetic inversion in monostatic ground penetrating radar: TEM horn calibration and application, IEEE Trans. Geosci. Remote Sens. 38 (4) (2000) 1936–1946.
[45] Y. Cao, J. Labuz, B. Guzina, Evaluation of pavement system based on ground-penetrating radar full-waveform simulation, Trans. Res. Rec. J. Trans. Res. Board 2227 (3) (2011) 71–78.
[46] S. Lambot, E.C. Slob, I. van den Bosch, B. Stockbroeckx, M. Vanclooster, Modeling of ground-penetrating Radar for accurate characterization of subsurface electric properties, IEEE Trans. Geosci. Remote Sens. 42 (11) (2004) 2555–2568.
[47] M.R. Mahmoudzadeh, J.B. Got, S. Lambot, C. Grégoire, Road inspection using full-wave inversion of far-field ground-penetrating radar data, in: Proceedings of the 7th International Workshop on Advanced Ground Penetrating Radar, Nantes, France, Jul. 2013, pp. 1–6.
[48] S. Busch, J. van der Kruk, J. Bikowski, H. Vereecken, Quantitative conductivity and permittivity estimation using full-waveform inversion of on-ground GPR data, Geophysics 77 (6) (2012) H79–H91.
[49] A. Tran, F. André, C. Craeye, S. Lambot, Near-field or far-field full-wave ground penetrating radar modeling as a function of the antenna height above a planar layered medium, Progress In Electromagnetics Research, vol. 141, pp. 415–430, 2013.
[50] F. Lavoué, R. Brossier, L. Métivier, S. Garambois, J. Virieux, Two-dimensional permittivity and conductivity imaging by full waveform inversion of multioffset GPR data: a frequency-domain quasi-Newton approach, Geophys. J. Int. 197 (1) (2014) 248–268.
[51] S. Lambot, F. André, Full-wave modeling of near-field radar data for planar layered media reconstruction, IEEE Trans. Geosci. Remote Sens. 52 (5) (2014) 2295–2303.
[52] A.P. Tran, F. André, S. Lambot, Validation of near-field ground-penetrating radar modeling using full-wave inversion for soil moisture estimation, IEEE Trans. Geosci. Remote Sens. 52 (9) (2014) 5483–5497.
[53] S. Lambot, L. Weihermller, J. Huisman, H. Vereecken, M. Vanclooster, E. Slob, Analysis of air-launched ground-penetrating radar techniques to measure the soil surface water content, Water Resour. Res. 42 (11) (2006) 1–12.
[54] J. Minet, S. Lambot, E. Slob, M. Vanclooster, Soil surface water content estimation by full-waveform GPR signal inversion in the presence of thin layers, IEEE Trans. Geosci. Remote Sens. 48 (3) (2010) 1138–1150.
[55] W. Huyer, A. Neumaier, Global optimization by multilevel coordinate search, J. Global Optim. 14 (4) (1999) 331–355.
[56] J.C. Lagarias, J.A. Reeds, M.H. Wright, P.E. Wright, Convergence properties of the nelder-mead simplex method in low dimensions, SIAM J. Optim. 9 (1) (1998) 112–147.
[57] J. Ledieu, P. De Ridder, P. De Clerck, S. Dautrebande, A method of measuring soil moisture by time-domain reflectometry, J. Hydrol. 88 (3–4) (1986) 319–328.
[58] S. Lambot, J. Rhebergen, I. van den Bosch, E. Slob, M. Vanclooster, Measuring the soil water content profile of a sandy soil with an off-ground monostatic ground penetrating radar, Vadose Zone J. 3 (4) (2004) 1063–1071.
[59] J.D. Rhoades, P.A.C. Raats, R.J. Prather, Effects of liquid-phase electrical conductivity, water content, and surface conductivity on bulk soil electrical conductivity1, Soil Sci. Soc. Am. J. 40 (5) (1976) 651–655.
[60] K. Jadoon, E. Slob, M. Vanclooster, H. Vereecken, S. Lambot, Uniqueness and stability analysis of hydrogeophysical inversion for time-lapse ground-penetrating radar estimates of shallow soil hydraulic properties, Water Resour. Res. 44 (W09421) (2008) 1–13.
[61] A. De Coster, A. Tran, S. Lambot, Fundamental analyses on layered media reconstruction using GPR and full-wave inversion in near-field conditions, IEEE Trans. Geosci. Remote Sens. 54 (9) (2016) 5143–5158.
[62] C. Grégoire, A. Van der Wielen, C. Van Geem, Determination of velocities with radar in road layers, in Proceeding of the 13th International Workshop on Advanced Ground Penetrating Radar (IWAGPR, 2015), Florence, Italy, Jul. 2015, pp. 1–4.
[63] M. Mahmoudzadeh, S. Lambot, Full-wave calibration of time- and frequency-domain ground-penetrating radar in far-field conditions, IEEE Trans. Geosci. Remote Sens. 52 (1) (2014) 664–678.